DIFFERENCES IN DEFECT DISTRIBUTION ACROSS SCAN STRATEGIES IN ELECTRON BEAM AM Ti-6Al-4V

The fraction and size of pores present in EBM Ti-6Al-4V specimens varies depending on the melting strategy used, whether linear raster melting or point melting.

Maria J. Quintana, Iowa State University, Ames, Universidad Panamericana, Mexico, and Center for Advanced Non-Ferrous Structural Alloys, an NSF I/UCRC

Katie O'Donnell, Iowa State University, Ames, and Center for Advanced Non-Ferrous Structural Alloys, an NSF I/UCRC

Matthew J. Kenney, Iowa State University, Ames

Peter C. Collins, Iowa State University, Ames, Center for Advanced Non-Ferrous Structural Alloys, an NSF I/UCRC, and Ames Laboratory, Iowa

In recent years, additive manufacturing (AM) has begun to displace traditional manufacturing techniques for specific applications. Notable benefits of AM include reduced times from design to product, an improved buy-to-fly ratio, lower waste, and the ability to produce complex geometries[1,2]. An additional benefit of additive manufacturing is the variety of manufacturing processes that span across heat source (e.g., laser, electron beam, plasma), input material type (e.g., powder, wire), atmosphere, and the number of axes of control among others[2-4]. This variability in processing route means that a process can be identified and optimized for a class of products or parts. Despite these various advantages, one of the primary drawbacks of AM processes is porosity within builds, which ultimately reduces the ability of a part to withstand tensile stresses and can lead to premature failure[4-6].

Electron beam melting (EBM) is a powder bed fusion technique that uses an electron beam as a heat source to melt powder particles that have been spread over a build plate[7]. Unlike laser-based processes, EBM requires the build chamber to be at vacuum, reducing the probability of porosity stemming from gases present within the build chamber[1]. Gas pores in EBM are thus typically caused by either gases present in the feedstock material (i.e., retained gas porosity) or vaporization of select elements (i.e., keyholing)[4,8]. Gas pores formed through either mechanism result in nearly spherical morphologies whose locations within the layer of a build and presence within a solidified part are influenced by the fluid dynamics of the melt pool[4,9,10].

The most common scan strategies of EBM are point-melting and variations on linear raster scan strategies, i.e., moving the electron beam in a linear fashion across the powder bed following a pattern[11]. Point-melting scan strategies, less commonly studied and used, involve point-by-point melting of small volumes of material of the powder bed. Research has shown that point-by-point melting strategies can be used for site-specific control of the resulting microstructure and texture by varying process parameters and the location and order of points melted, thereby leading to local and specific variations in mechanical properties[12,13].

OBSERVATIONS IN AS-BUILT SAMPLES

Ti-6Al-4V specimens were produced at Oak Ridge National Laboratory Manufacturing Demonstration Facility using an ARCAM EBM Q10plus system and TEKNA Ti-6Al-4V plasma atomized powder. Each specimen had a geometry of 15 x 15 x 25 mm.

Three different scan strategies were used to produce the samples: a linear raster scan (L), random point-melting (R), and what is known as the Dehoff point-melting strategy (D). The raster scan L consisted of a serpentine pattern that rotated 67.5° after the end of every layer. Each 15 x 15 mm area of R and D was segmented into coordinates. A computer-generated random

function was used for R, to assure every coordinate (or point) was melted only once and all coordinates were melted every layer. The Dehoff (D) strategy requires melting in an ordered manner by organizing the coordinates into arrays and subarrays and following a specific order. More information about all three of these scan strategies can be found in M. Quintana[14], M. Kirka[15], and P. Nandwanda[16]. The layer thickness was 50 µm for all strategies, and all samples were printed at the same time on a stainless steel build plate. Samples were imaged using an FEI Teneo LoVac field-emission scanning electron microscope (SEM). Images were then analyzed using MIPAR image analysis software.

Analysis of internal planes of the samples resulted in the spherical (gas) pore data presented in Table 1 and Figs. 1 and 2. The raster scan strategy (L) had three times as many pores as either of the two point-melting strategies. All spherical pores over 25 µm were only observed in the L sample, meaning the selected strategy has a large influence in both the number of pores formed and their sizes. The distribution of pores relative to build height in each sample was also assessed (Fig. 2) by classifying pores as belonging to one of three equal sized bins (each ~8.3 mm in height, labeled top, middle, and bottom). Samples R and L have a uniform distribution throughout the sample, while D has slightly fewer pores in the middle and more in the bottom.

Porosity is, by nature, very common in AM builds, and because pores are typically considered defects, research has been done to optimize AM parameters to minimize both the volume fraction and the size of pores in final parts[17,18]. As expected, the measurements of small amounts of porosity in the samples show both large standard deviations (Table 1) and a broad range of pore diameters. A comparison between the samples (strategies) can provide insights into the influence of melt pool morphologies and process parameters on the sizes of gas pores.

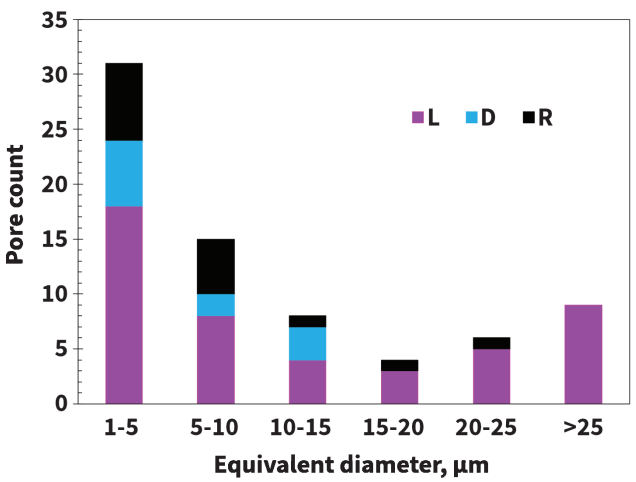

Fig. 1 — Equivalent diameter distribution of the spherical pores across the three strategies (L, D, and R) observed in one internal plane (15 x 25 mm).

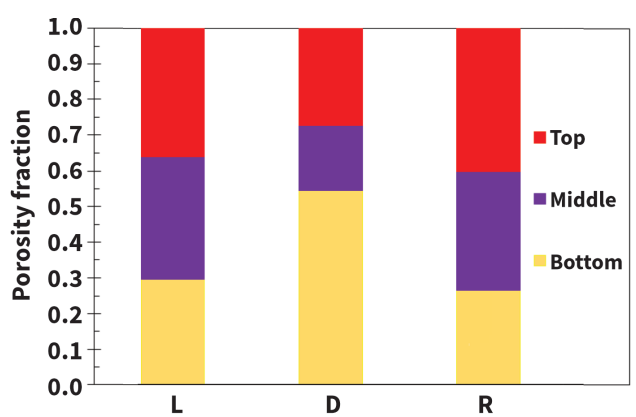

Fig. 2 — Distribution of spherical porosity across raster, Dehoff, and random strategies sub-separated into top, middle, and bottom regions within each sample.

FLUID DYNAMICS IN AM MELT POOLS

Melt pool fluid dynamics can be divided into two general stages: first, the powder initially interacts with the heat source and melts, creating a region ruled by thermocapillary forces; and second, the heat source moves away and the melt pool begins to cool, switching the dominating force from thermocapillary to drag. Thermocapillary forces move pores in the direction of the thermal gradient, which, in the case of both raster and point-melting strategies, will bring pores to the surface of the melt pools[4]. As the melt pool cools, the thermal gradient is reduced, which in turn reduces the magnitude and influence of the thermocapillary force and makes drag the driving and dominant force (particularly in the tail end of the elongated raster melt pool). Fluid flow no longer drives pores to the surface and instead they are trapped inside the liquid material[4]. In other words, pores are more easily eliminated from the leading edge of a raster melt pool, as opposed to the tail end, as a result of thermocapillary forces dominating over drag forces.

Notably, because the heat source does not move during the residence time in point-melting strategies, the melt pool does not develop a trailing region (i.e., a "tail"), and instead is by

TABLE 1 – STATISTICS OF SPHERICAL PORES: ANALYSIS OF ONE INTERNAL PLANE FOR EACH STRATEGY

Scanning strategy	Pore count	Area fraction*	Equivalent diameter (µm)		
			Average	Standard deviation	Range
L	47	0.0000433	14.20	13.55	1.6-51.7
R	15	0.0000028	7.17	5.20	2.8-20.1
D	11	0.0000018	6.97	4.74	2.2-14.8

**Area fraction is based on a sectioned surface of 15 x 25 mm.*

and large consistently the leading edge of a raster melt pool. Though research into the fluid dynamics in point melting is scarce, parallels can be drawn from publications on laser spot welding[19], where Marangoni convection (i.e., thermocapillary forces) dominates melt pool thermodynamics. Thermal gradients within individual melt pools are therefore higher in point-melting strategies compared to linear raster with elongated melt pools. Higher thermal gradients allow thermocapillary forces to dominate the fluid flow through a greater relative volume of each melt pool and eliminate some of the gas porosity present in the melt pools by dragging them to the surface where they are eliminated.

Melt pool fluid dynamics and the ability of gas bubbles to escape the melt pool are not influenced by location (in a plane) or by height, as observed in the L, D, and R samples, only by varying the scanning strategy. Thermal gradients within AM parts are known to vary along the height of a part, based on thermal conductivity through the build plate as opposed to the surrounding powder bed, pre-heat temperatures, time at temperature, and the number of layers above a selected region, among other factors[2,14]. These thermal gradient variations affect thermal (and thermomechanical) gyrations and corresponding phase transformations, which results in notable differences in the resulting microstructure[2,14]. The fact that no significant variation in spherical porosity was observed along the build height suggests that the best time for gas pores to escape is during initial melting, either while the electron beam is centered on the melt pool or immediately after, particularly for point-melting strategies.

INDUSTRIAL RELEVANCE

While some of the typically undesirable attributes of AM builds (e.g., residual stress and surface roughness) can be mitigated with post-processing or concurrent hybrid-processing steps (e.g., annealing, in-situ or ex-situ machining)[2], porosity, on the other hand, is difficult to eliminate with these methods[4,16]. Porosity is detrimental in all structural metals, as all pores act as stress concentrators and can lead to premature failure[1,2,6,20]. Investigations into optimizing processing parameters to reduce porosity in powder bed fusion (PDF) AM techniques are common[1,4,5], but tend to focus on power and scan speed and rarely venture into differing scan strategies.

In AM builds, the size of the gas pores ranges considerably, from tens of microns (Fig. 3a) to less than 5 microns (Fig. 3b). The smaller pore sizes are more commonly observed in the point-melting scans. With low volume fractions of porosity, it can be difficult to determine accurately the amount and size of porosity. Knowledge of the size of gas pores is critical, as large pores (Fig. 3a) will lead to a larger local loss of tensile properties than smaller pores.

As mentioned, post-processing steps, typically in the form of heat treatments, are usually not successful at removing all pores in as-built parts[2,4,16]; thus, methods of reducing and eliminating porosity during the build process itself is preferable and the most effective route to ensure the final mechanical performance of a part is as expected during the design process. This work provides analysis on strategies which mitigate porosity (i.e., point-melting strategies are better than raster scans at eliminating porosity and reducing the size of the pores present) as a result of the forces dominating different stages of the melt pool fluid dynamics.

CONCLUSIONS

Observations of the spherical porosity in EBM Ti-6Al-4V builds have shown a clear difference in the resulting fraction and the size of pores present between a linear raster-melting strategy and point-melting strategies (Dehoff and random). Whether as a result of retained gas porosity from the powder, or vaporized elements in the build, samples from all three melting strategies present gas porosity. Fewer spherical gas pores were observed in both of the point-melting EBM scan strategies as opposed to the prototypical, and widely used, linear raster melting scan strategy. Point-melting strategies also resulted in spherical gas pores with an average diameter of half the size of the average diameter of pores in the raster-melting strategy. Pores with a diameter greater than 25 µm were only observed in the L sample.

Gas pores are neither preferentially formed nor retained at any particular height of the sample, leading to the

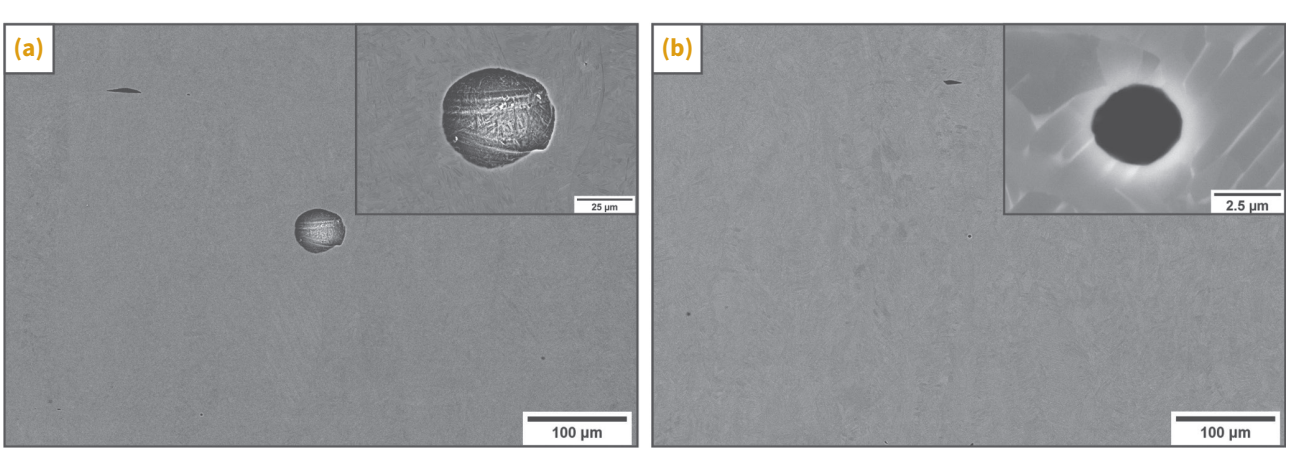

Fig. 3 — Spherical pores observed in EBM samples obtained with different scanning strategies: (a) linear raster scan-L and (b) point-melting scan-R.

conclusion that it is the fluid dynamics of the melt pools and not the thermal gyrations generated by the parameters that most strongly influences the ability of gas bubbles to escape the melted material during the AM process.

This difference can be attributed to the nature and morphology of the melt pools and the fluid dynamics from point-melting strategies, compared to the relatively larger and elongated melt pools that form in raster-melting strategies that contain two very distinct fluid dynamics domains, with opposing driving forces. Melt pools in point-melting strategies are almost exclusively dominated by Marangoni convection, whereas raster-melting strategies also contain a tail end to the melt pool that is dominated by drag forces. **~AM&P**

For more information: Peter Collins, professor, Iowa State University, 2220 Hoover Hall, 528 Bissell Rd., Ames, IA, 50011, 515.294.5127, pcollins@iastate.edu, https://www.mse.iastate.edu/pcollins/.

Acknowledgment

The research is sponsored by the Department of the Navy, Office of Naval Research under ONR award number N00014-18-1-2794. Any opinions, findings, and conclusions or recommendations expressed in this material are those of the author(s) and do not necessarily reflect the views of the Office of Naval Research.

Access to the Oak Ridge National Laboratory's (ORNL) additive manufacturing equipment at ORNL's Manufacturing Demonstration Facility (MDF) was facilitated by U.S. Department of Energy's Strategic Partnership Projects (SPP) mechanism. More information can be found at https://science.energy.gov/lp/strategic-partnership-projects. Research sponsored by the U.S. Department of Energy, Office of Energy Efficiency and Renewable Energy, Industrial Technologies Program, under contract DE-AC05-00OR22725 with UT-Battelle LLC.

References

1. S. Tammas-Williams, et al., XCT Analysis of the Influence of Melt Strategies on Defect Population in Ti–6Al–4V Components Manufactured by Selective Electron Beam Melting, *Materials Characterization*, 102, p 47-61, 2015.

2. T.D. Ngo, et al., Additive Manufacturing (3D Printing): A Review of Materials, Methods, Applications and Challenges, *Composites Part B: Engineering,* Vol 143, p 172-196, 2018.

3. M. Kottman, et al., Laser Hot Wire Process: A Novel Process for Near-net Shape Fabrication for High-throughput Applications, *JOM, 67*(3), p 622-628, 2015.

4. S.M.H. Hojjatzadeh, et al., Pore Elimination Mechanisms During 3D Printing of Metals, *Nature Communications, 10*(1), p 1-8, 2019.

5. M. Tang, P.C. Pistorius, and J.L. Beuth, Prediction of Lack-of-fusion Porosity for Powder Bed Fusion, *Additive Manufacturing,* 14, p 39-48, 2017.

6. S. Liu and Y.C. Shin, Additive Manufacturing of Ti6Al4V Alloy: A Review, *Materials & Design,* 164, 107552, 2019.

7. H. Chen, et al., Powder-spreading Mechanisms in Powder-bed-based Additive Manufacturing: Experiments and Computational Modeling, *Acta Materialia,* 179, p 158-171, 2019.

8. P. Ferro, et al., A Modified Volumetric Energy Density–based Approach for Porosity Assessment in Additive Manufacturing Process Design, *The International Journal of Advanced Manufacturing Technology, 110*(7), p 1911-1921, 2020.

9. D. Du, et al., Influence of Static Magnetic Field on Microstructure and Mechanical Behavior of Selective Laser Melted AlSi10Mg Alloy, *Materials & Design,* 181, 107923, 2019.

10. X. Wang and K. Chou, Effects of Thermal Cycles on the Microstructure Evolution of Inconel 718 During Selective Laser Melting Process, *Additive Manufacturing,* 18, p 1-14, 2017.

11. D.Ding,etal.,ATool-pathGen-eration Strategy for Wire and Arc Additive Manufacturing, *The International Journal of Advanced Manufacturing Technology, 73*(1-4), p 173-183, 2014.

12. R.R. Dehoff, et al., Site Specific Control of Crystallographic Grain Orientation through Electron Beam Additive Manufacturing, *Materials Science and Technology, 31*(8), p 931-938, 2015.

13. N. Raghavan, et al., Localized Melt-scan Strategy for Site Specific Control of Grain Size and Primary Dendrite Arm Spacing in Electron Beam Additive Manufacturing, *Acta Materialia,* 140, p 375-387, 2017.

14. M.J. Quintana, et al., Texture Analysis of Additively Manufactured Ti-6Al-4V Deposited using Different Scanning Strategies, *Metallurgical and Materials Transactions A,* p 1-10, (2020).

15. M.M. Kirka, et al., Strategy for Texture Management in Metals Additive Manufacturing, *JOM, 69*(3), p 523-531, 2017.

16. P. Nandwana and Y. Lee, Influence of Scan Strategy on Porosity and Microstructure of Ti-6Al-4V Fabricated by Electron Beam Powder Bed Fusion, *Materials Today Communications,* 100962, 2020.

17. B. Zhang, S. Liu, and Y.C. Shin, In-Process Monitoring of Porosity during Laser Additive Manufacturing Process, *Additive Manufacturing,* 28, p 497-505, 2019.

18. K. Moussaoui, et al., Effects of Selective Laser Melting Additive Manufacturing Parameters of Inconel 718 on Porosity, Microstructure and Mechanical Properties, *Materials Science and Engineering: A,* 735, 182-190, 2018.

19. X. He, P.W. Fuerschbach, and T. DebRoy, Heat Transfer and Fluid Flow during Laser Spot Welding of 304 Stainless Steel, *Journal of Physics D: Applied Physics, 36*(12), 1388, 2003.

20. J.M. Boileau and J.E. Allison, The Effect of Solidification Time and Heat Treatment on the Fatigue Properties of a Cast 319 Aluminum Alloy, *Metallurgical and Materials Transactions A, 34*(9), p 1807-1820, 2003.